Nano-Micro Letters

ISSN 2311-6706
e-ISSN 2150-5551
CN 31-2103/TB

ARTICLE

https://doi.org/10.1007/s40820-020-0405-7

Cite as
Nano-Micro Lett.
(2020) 12:78

Received: 15 December 2019
Accepted: 2 February 2020
Published online: 25 March 2020

Partial Atomic Tin Nanocomplex Pillared Few-Layered $Ti_3C_2T_x$ MXenes for Superior Lithium-Ion Storage

Shunlong Zhang[1], Hangjun Ying[1], Bin Yuan[2,3], Renzong Hu[2,3], Wei-Qiang Han[1] ✉

Shunlong Zhang and Hangjun Ying have contributed equally to this work.

✉ Wei-Qiang Han, hanwq@zju.edu.cn

[1] School of Materials Science and Engineering, Zhejiang University, 310027 Hangzhou, People's Republic of China

[2] School of Materials Science and Engineering, South China University of Technology, 510641 Guangzhou, People's Republic of China

[3] Key Laboratory of Advanced Energy Storage Materials of Guangdong Province, 510641 Guangzhou, People's Republic of China

HIGHLIGHTS

- A facile NH_4^+ method was proposed to prepare Sn nanocomplex pillared few-layered $Ti_3C_2T_x$ MXene nanosheets.
- The MXene nanosheets showed excellent lithium-ion storage performances among MXene-based materials, which can maintain 1016 mAh g^{-1} after 1200 cycles at 2000 mA g^{-1} and deliver a stable capacity of 680 mAh g^{-1} at 5 A g^{-1}.

ABSTRACT MXenes have attracted great interest in various fields, and pillared MXenes open a new path with larger interlayer spacing. However, the further study of pillared MXenes is blocked at multilayered state due to serious restacking phenomenon of few-layered MXene nanosheets. In this work, for the first time, we designed a facile NH^{4+} method to fundamentally solve the restacking issues of MXene nanosheets and succeeded in achieving pillared few-layered MXene. Sn nanocomplex pillared few-layered $Ti_3C_2T_x$ (STCT) composites were synthesized by introducing atomic Sn nanocomplex into interlayer of pillared few-layered $Ti_3C_2T_x$ MXenes via pillaring technique. The MXene matrix can inhibit Sn nanocomplex particles agglomeration and serve as conductive network. Meanwhile, the Sn nanocomplex particles can further open the interlayer spacing of $Ti_3C_2T_x$ during lithiation/delithiation processes and therefore generate extra capacity. Benefiting from the "pillar effect," the STCT composites can maintain 1016 mAh g^{-1} after 1200 cycles at 2000 mA g^{-1} and deliver a stable capacity of 680 mAh g^{-1} at 5 A g^{-1}, showing one of the best performances among MXene-based composites. This work will provide a new way for the development of pillared MXenes and their energy storage due to significant breakthrough from multilayered state to few-layered one.

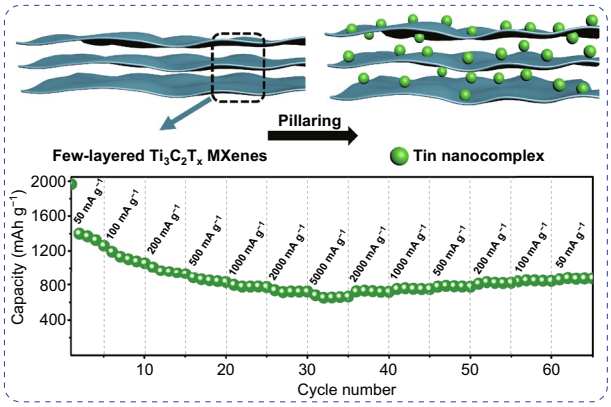

KEYWORDS Pillared MXene; Few-layered MXene; Tin nanocomplex; Lithium-ion storage

1 Introduction

Two-dimensional (2D) materials have stimulated great research interest in the fields of energy storage, catalysis, sensor, semiconductor, etc, because of their novel physical and chemical properties [1–4]. MXenes are a new family of 2D transition metal carbides and nitrides discovered in 2011 [4, 5]. They can be prepared by selectively etching "A" atomic layers from 3D layered MAX phases ($M_{n+1}AX_n$, where *M* is an early transition metal, A is an IIIA or IVA group element, $n = 1$, 2, 3, and X is C and/or N) [6, 7]. The final chemical formula of MXenes can be denoted as $M_{n+1}X_nT_x$; the meaning of each letter is the same as that of MAX phases ($M_{n+1}AX_n$), except for T_x representing terminated –OH, –F, and –O functional groups at surface [8, 9].

Although MXenes show promising application prospect in energy storage [10–12], the practical electrochemical performance of MXenes falls short of expectations [13]. This poor result is probably due to the blocking effect of surface anion and excessive accumulation of layers [14–16]. In order to improve the electrochemical performance of MXenes, many modification strategies have been carried out, including increasing the interlayer spacing by insertion of other agents [17–19], constructing 3D morphology [20, 21], and creating porous structure [22, 23]. The first modification strategy of enlarging interlayer spacing has been proved an effective method to improve the capacities of MXenes, and it is figuratively called "pillaring" technique. The pillaring agents could be small molecular cations [24], cationic surfactant [25], polymers [26], metal nanocomplex [27], and so on. Figure S1 shows the development history of pillaring technique in MXene-based electrode materials. In detail, the interesting pillared MXenes with active materials date back to 2016, and then, a series of works about pillared MXenes were reported from different perspectives, including various intercalation agents (CTAB [25], KOH [17]), active materials (Sn [25, 28, 29], Co [15], S [18]), and different battery systems [18, 25, 30]. Due to "pillar effect," which means the interlayer spacing of MXene matrix was enlarged by active materials, providing more lithium storage interspace and endowing the pillared MXene nanocomposites excellent electrochemical performance [25, 28]. Unfortunately, up to now, all of these reports were blocked at the state of multilayered MXenes with thickness about 5 μm, corresponding to about 5000 layers calculated on the interlayer spacing of ~ 1 nm (Fig. S2) [13]. Particularly, due to serious restacking issues of few-layered MXene nanosheets [31, 32], there is no report about pillared few-layered MXene composites. It is well known that few-layered structure is considered to benefit the electrochemical properties of 2D materials [33–35]. Therefore, discovering effective method to prepare pillared few-layered MXene-based composites is of great significance; realization of pillared few-layered MXenes with active materials is still a big challenge to be taken.

Herein, for the first time, we synthesized atomic Sn nanocomplex pillared few-layered $Ti_3C_2T_x$ (STCT) composites via pillaring technique with the assistance of NH_4^+ method and investigated its electrochemical properties as anodes for lithium-ion battery, effectively solving the restacking phenomenon of few-layered MXenes. Notably, benefiting from the few-layered nanosheet structure and pillared ultra-large interlayer spacing, the STCT composites exhibit significant improvement in electrochemical performance. It delivers outstanding cycling stability with a capacity retention of 1016 mAh g^{-1} after 1200 cycles and superb rate ability with a capacity retention of 680 mAh g^{-1} at 5 A g^{-1}. The electrochemical performance is even superior than that of the pillared multilayered MXenes with low formula weights [15, 17], although the related theoretical study indicates that MXenes with low formula weights (such as V_2C, Ti_2C) show more promising prospect in energy storage than the ones with high formula weights [36]. The results strongly demonstrate the advantages of pillared few-layered MXenes in the field of energy storage.

2 Experimental Section

2.1 Synthesis Methods

2.1.1 Synthesis of Multilayered $Ti_3C_2T_x$ MXenes

Commercial Ti_3AlC_2 powders (98% in purity) were purchased from Beijing Forsman Technology Company. The multilayered $Ti_3C_2T_x$ MXene powders can be easily obtained according to previous report [28].

2.1.2 Synthesis of Few-layered $Ti_3C_2T_x$ MXenes (NH^{4+} Method)

Multilayered $Ti_3C_2T_x$ MXene powders (1 g) were immersed into 10 mL aqueous solution of tetramethylammonium

https://doi.org/10.1007/s40820-020-0405-7

hydroxide (25 wt%, TMAOH) and stirred at room temperature for 24 h. Organic molecules were intercalated into the interlayer of MXenes, and then, the intercalated multilayered $Ti_3C_2T_x$ MXenes were collected by centrifugation and washed with deionized (DI) water for three times. The final precipitation was dispersed in 50 mL DI water for ultrasonic treatment at atmosphere of argon gas. After ultrasonication for 1 h, the supernatant was collected for subsequent usage via centrifugation at speed of 3500 r min^{-1} for 10 min, and the precipitation was again dispersed in 50 mL DI water for further ultrasonic treatment, and the above process was repeated for 4 times. Then, all the above-mentioned supernatants were collected together with nearly volume of 200 mL. In order to reduce water volume, shorten working time of freeze-drying process and avoid the restacking phenomenon of few-layered MXene nanosheets, 20 mL ammonia water (28%) or 25 mL ammonium bicarbonate aqueous solution (0.5 mol L^{-1}) was added into the MXene supernatants, and an obvious electrostatic flocculation phenomenon can be observed. After resting for 1 h, the flocculation settles down automatically and can be collected. Few-layered $Ti_3C_2T_x$ MXene powders can be obtained by freeze-drying of the flocculation and subsequent annealing treatment (180 °C, 6 h) with Ar atmosphere. Since the above-mentioned preparation process of few-layered MXene powders was first time proposed, we termed it as NH^{4+} method, which was first time put forward and can fundamentally solve restacking issues of few-layered MXene nanosheets. It should be noted that the other ammonium salts are also suitable for electrostatic flocculation process.

2.1.3 Synthesis of CTAB-$Ti_3C_2T_x$ MXenes

The CTAB-$Ti_3C_2T_x$ MXenes were prepared by treating $Ti_3C_2T_x$ MXene powders in hexadecyl trimethyl ammonium bromide (CTAB) solutions as reported [28].

2.1.4 Synthesis of STCT Composites

As-prepared multilayered or few-layered $Ti_3C_2T_x$ MXene powders (0.3 g) were immersed into 40 mL 0.2 wt% CTAB solution and stirred for 24 h at 40 °C, then 2.6 g $SnCl_4 \cdot 5H_2O$ was added and mixed solution was stirred again for 24 h for ion-exchange process, and the final product of Sn nanocomplex pillared few-layered $Ti_3C_2T_x$ (STCT) composites can be obtained after centrifugation (3500 r min^{-1}, 10 min), freeze-drying, and annealing treatment in Ar atmosphere (180 °C, 2 h). Note that STCT composites are at few-layered state in this manuscript unless otherwise specified.

2.2 Material Characterization

X-ray diffraction (XRD) measurements were taken by Shimadzu XRD 6000 with Cu Ka radiation in the range of $2\theta = 3°–90°$. AFM results were collected by Oxford Cypher S to detect the height of the nanosheets. The microstructure of the as-prepared samples was measured by field emission scanning electron microscopy (FESEM, Hitachi, SU8010) and transmission electron microscopy (TEM, FEI Ltd, Tecnai F20). X-ray photoelectron spectroscopy (XPS) analysis was carried out in Thermo Fisher 250XI to investigate chemical bonds of the samples. The discharged electrodes were washed with fresh dimethyl carbonate (DMC) solvent to remove surficial residuals before related characterization.

2.3 Electrochemical Measurements

Coin type cells (2032) were assembled in argon-filled glove box using STCT composites as working electrodes and Li foil as the negative electrode. The electrodes were prepared with mixed STCT composites, super-P, and carboxyl methyl cellulose (CMC) to form slurry at the weight ratio of 7:1:2. Cyclic voltammogram (CV) curves at different scan rates between 0.01 and 3.0 V were obtained, and batteries were also analyzed by EIS measurements using Solartron 1470E Electrochemical Interface (Solartron Analytical, UK). Cycling performance and discharging/charging measurements were carried out on LAND battery test system.

3 Results and Discussion

The preparation process of samples is illustrated in Fig. 1. Briefly, few-layered $Ti_3C_2T_x$ MXene powders were prepared via NH_4^+ method, which can fundamentally solve the restacking issues of few-layered MXene nanosheets, and the detailed process can be seen in experimental section. Followed by CTAB pre-pillaring, ion-exchange insertion, and Sn^{4+} pillaring process, we finally obtained Sn nanocomplex pillared few-layered $Ti_3C_2T_x$ (STCT) composites

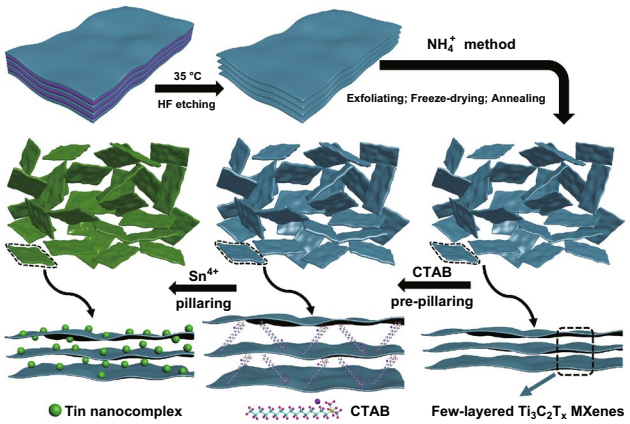

Fig. 1 Schematic illustration of the preparation procedure of Sn nanocomplex pillared few-layered $Ti_3C_2T_x$ (STCT) composites by etching, sonication, pre-pillaring, and pillaring processes

with few-layered structure. In contrast, multilayered $Ti_3C_2T_x$ is obtained via HF etching without subsequent process (Fig. S3). Because of the delicate properties and structures, it is difficult to effectively prepare powders of few-layered MXenes from colloids after exfoliation process (Fig. S4). In this work, for the first time, we employed electrostatic flocculation of NH_4^+ method to prepare few-layered $Ti_3C_2T_x$ nanosheet powders. Due to absorbed T_x groups, MXene nanosheet is negatively charged, which is also one of the basic properties of MXene colloids and consistent with the result of zeta potential test (Fig. S5) [37]. MXene nanosheets can be uniformly dispersed in colloidal state because of electrostatic repulsion among different nanosheets. The $Ti_3C_2T_x$ nanosheets settle down after the addition NH_4^+ solution owing to destruction of electrostatic equilibrium state of the MXene nanosheets (Fig. S6a–e), leading to formation of flocculation [38], and the yield is considerable after freeze-drying of flocculation and annealing process (Fig. S7), ranging from 50 to 70% (Figs. S6f–g and S9).

The structure of materials in different steps is identified by XRD and exhibited in Figs. 2 and S8 with different diffraction angle ranges. There is an obvious shift in the main peak of (002), which explains well the change of interlayer spacing [25, 28, 38]. As shown in Fig. 2a, b, the disappearance of main peak (104) at 39° of Ti_3AlC_2 after HF etching suggests the complete etching of Al layer, and the left shift of peak (002) indicates enlarged interlayer spacing [6]. After immersing few-layered $Ti_3C_2T_x$ in CTAB solution for hours, the main peak of $Ti_3C_2T_x$ shifts dramatically to a lower angle, implying the high pillaring ability of cationic surfactant [25]. The intense diffraction peaks centered at 4° further confirm the successful intercalation of CTAB into the interlayers of $Ti_3C_2T_x$ (Fig. 2c). Afterward, with the insertion of Sn nanocomplex via ion exchange based on Sn^{4+}, the main peak of STCT composites shifts to a higher angle, which indicates the CTAB is replaced by Sn nanocomplex particles with small volume, resulting in interlayer

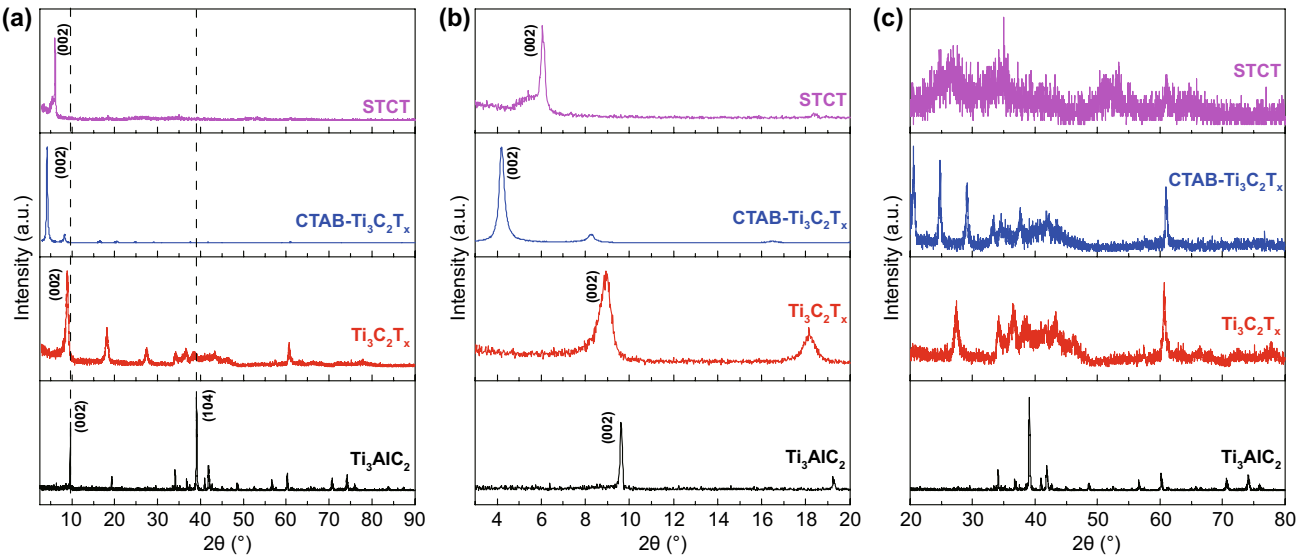

Fig. 2 XRD patterns of Ti_3AlC_2, $Ti_3C_2T_x$, CTAB-$Ti_3C_2T_x$, and STCT composites at different diffraction angle ranges: **a** 2 theta from 3° to 90°, **b** 2 theta from 3° to 20°, and **c** 2 theta from 20° to 80°

https://doi.org/10.1007/s40820-020-0405-7

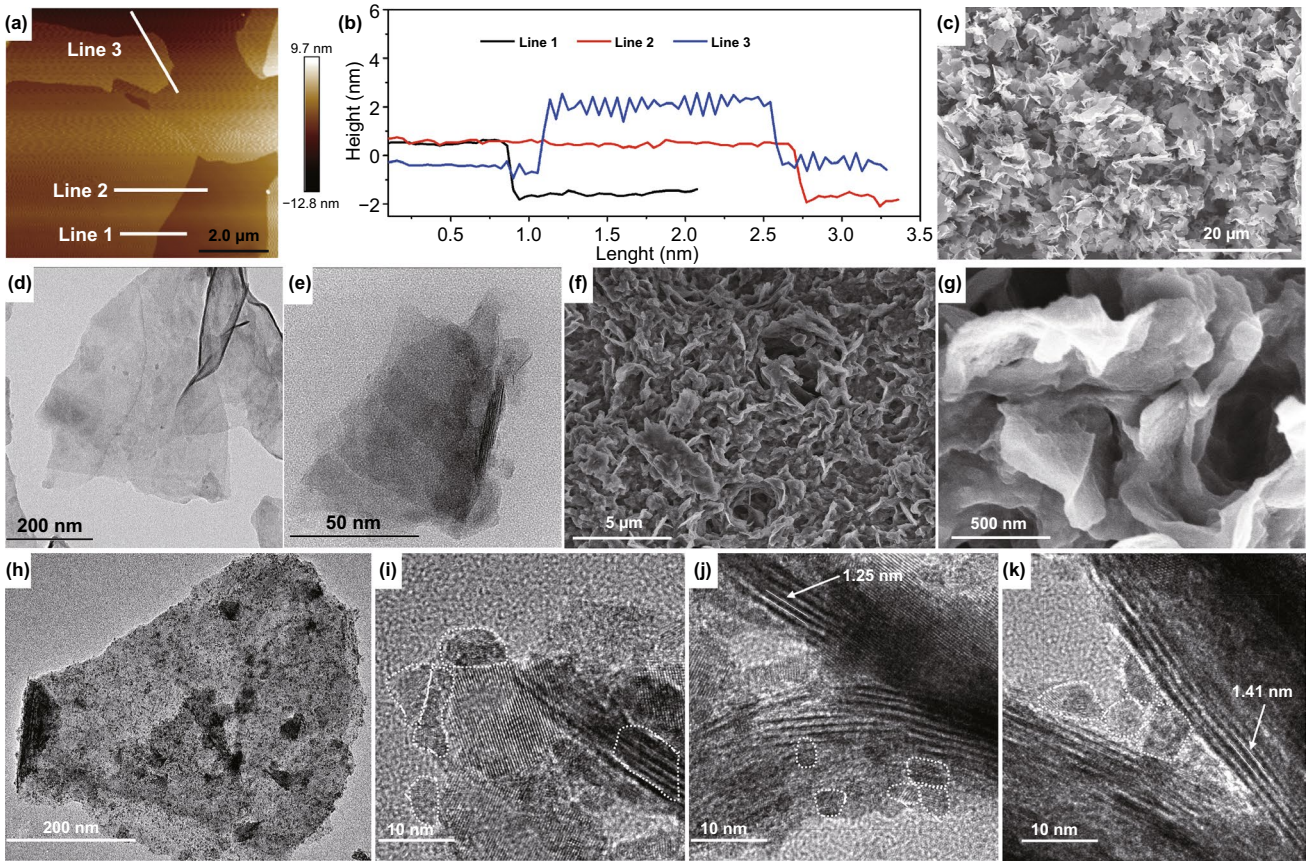

Fig. 3 Characterization of few-layered $Ti_3C_2T_x$ and STCT composites. **a, b** AFM images, **c** SEM image, and **d, e** TEM images of few-layered $Ti_3C_2T_x$. **f, g** SEM images and **h–k** TEM images of STCT composites

spacing diminution [25]. As shown in Fig. 2c, the broad peaks corresponding to Sn nanocomplex are concealed by the intense diffraction peak of $Ti_3C_2T_x$ MXenes.

As shown in Fig. 3a, b, the few-layered structure of $Ti_3C_2T_x$ can be confirmed by AFM test. The scanned profile height of nanosheets indicates the number of layers of MXenes is about 2 or 3, demonstrating successful preparation of few-layered $Ti_3C_2T_x$ MXene powders, which show obvious nanosheet structure with microscale size in *ab* plane. The uniform nanosheet morphology without agglomeration can be further testified by SEM images at different magnifications (Fig. S10 and Fig. 3c). The translucent state under transmission electron beam confirms the few-layered structure of $Ti_3C_2T_x$ (Fig. 3d, e). The slight curl morphology indicates the flexibility of few-layered $Ti_3C_2T_x$ MXene nanosheets. As the SEM images of STCT composites are shown in Fig. 3f, g, the lamellar structure remains in comparison with $Ti_3C_2T_x$; nevertheless, the thickness of $Ti_3C_2T_x$ slice increases slightly, suggesting the successful decoration of Sn nanocomplex. For better observation, the multilayered $Ti_3C_2T_x$ is also pillared. As shown in Fig. S11, the interlayer space is padded by small particles, further confirming the Sn nanocomplex pillaring in $Ti_3C_2T_x$ interlayers. TEM image in Fig. 3h clearly reveals the uniform distribution of Sn nanocomplex dots in the few-layered $Ti_3C_2T_x$ matrix. The HRTEM images further exhibit the detailed distributed situation of Sn nanocomplex dots (Fig. 3i–k). The small Sn nanocomplex particles about 3–5 nm were anchored tightly at surface of $Ti_3C_2T_x$, and ultrasmall atomic Sn nanocomplex dots were intercalated into the interlayers of $Ti_3C_2T_x$ [15] or within the inner side of V-like construction between nanosheets. CTAB acts as pre-pillaring agent and surface-stabilizing agent, which effectively inhibits Sn nanocomplex particle growth and agglomeration [39]. The interlayer spacing of few-layered $Ti_3C_2T_x$ is sizeable after CTAB pre-pillaring, which provides enough space for accommodating

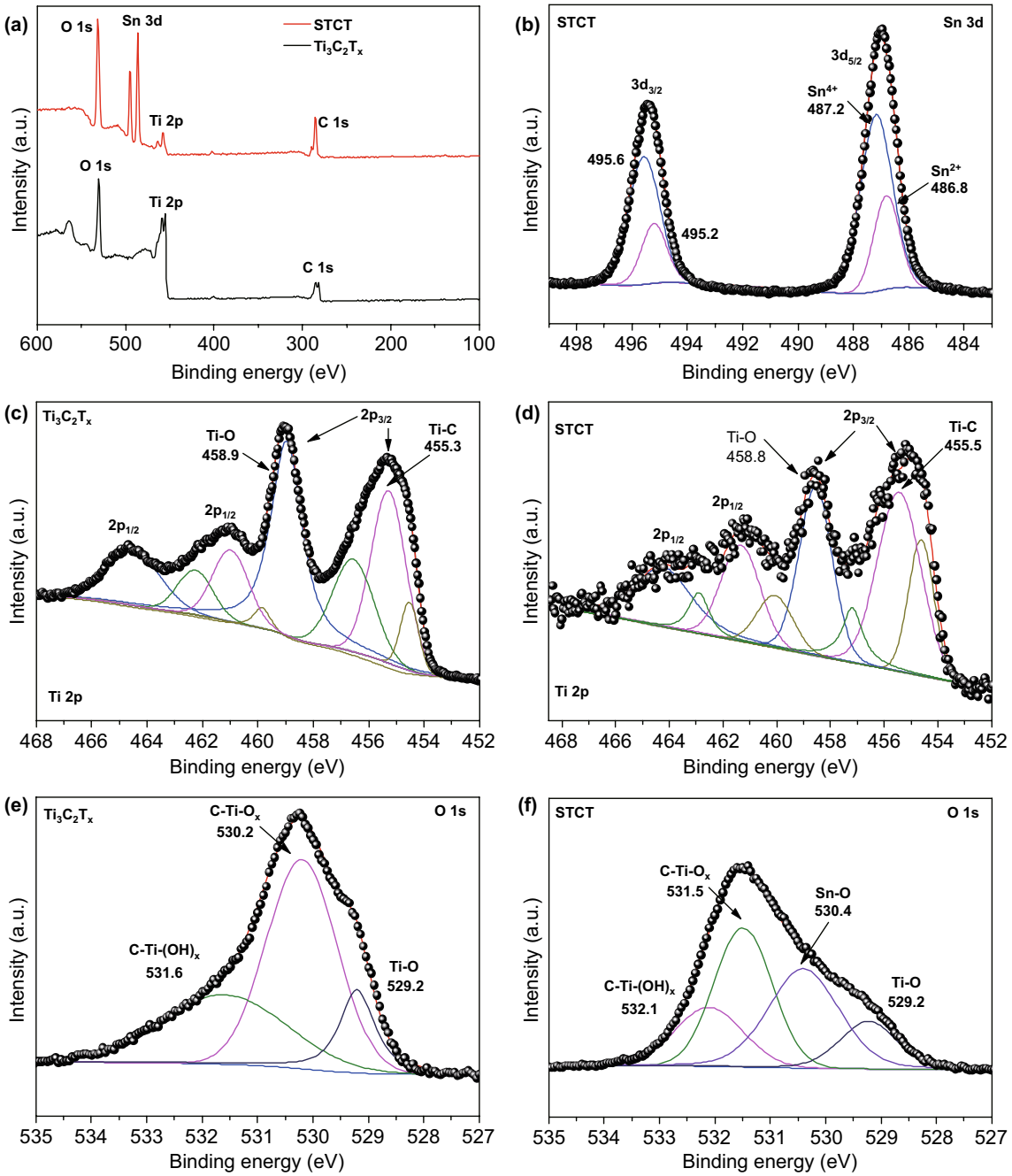

Fig. 4 XPS spectra of **a** $Ti_3C_2T_x$ and STCT composites, **b** high-resolution Sn 3d spectrum of STCT, **c–d** high-resolution Ti 2p spectra of $Ti_3C_2T_x$ and STCT, and **e, f** high-resolution O 1 s spectra of $Ti_3C_2T_x$ and STCT

Sn nanocomplex dots (Fig. S12). The interlayer spacing further restricts grain growth and insures the ultrasmall Sn nanocomplex size.

The chemical bonding is collected by XPS. The full spectra comparison (Fig. 4a) of individual $Ti_3C_2T_x$ and STCT composites further verifies the successful decoration of Sn nanocomplex. The detailed analysis shows that the Sn 3d peak consists of two primary peaks centered at 495.4 and 487.0 eV, attributed to the Sn $3d_{3/2}$ and $3d_{5/2}$, respectively. These two peaks can be deconvoluted into two pairs of peaks

https://doi.org/10.1007/s40820-020-0405-7

corresponding to Sn^{2+} and Sn^{4+}, respectively, indicating the incomplete oxidation state of Sn nanocomplex [40, 41] (Fig. 4b). As shown in Fig. 4c, d, the Ti 2p peaks of $Ti_3C_2T_x$ and STCT composites consist of four primary peaks, of which the two peaks with higher binding energy belong to Ti $2p_{1/2}$, while the lower two belong to Ti $2p_{3/2}$. These four peaks can be further split into eight peaks, respectively, corresponding to Ti^{2+}, Ti^{3+}, Ti–O, and Ti–C peaks [40, 42]. The O 1 s peak of $Ti_3C_2T_x$ can be deconvoluted into three peaks, respectively, matched to the C–Ti–$(OH)_x$, C–Ti–O_x, and Ti–O peaks [42]. However, for the STCT composites, a peak corresponding to Sn–O bond (530.4 eV) emerges, indicating the bonding between Sn oxide particles with the terminating groups (such as –OH, –O) at the surface of $Ti_3C_2T_x$ matrix [40]. In addition, slight shift of Ti $2p_{3/2}$ and O 1 s to higher binding energy also implies the forming of strong attraction between Sn nanocomplex and $Ti_3C_2T_x$ matrix [28]. As shown in Fig. S13, the sharp decline of C–Ti peak intensity and emergence of C=O peak further indicate the formation of chemical binding between Sn nanocomplex particles and $Ti_3C_2T_x$ matrix. The formation of interfacial Sn–O–Ti bonds can grant robust structure of the pillared composites, thereby assuring a stable electrochemical performance of STCT composites.

In order to evaluate electrochemical performance of STCT composites, we assembled 2032 type coin cell using lithium metal foil as counter electrode. As shown in Fig. 5a, the CV curves of STCT composites were measured between 0.01 and 3 V. The cathodic and anodic current response can be attributed to the electrochemical reactions between lithium ions and Sn nanocomplex as well as $Ti_3C_2T_x$ matrix. The redox peak current positions are consistent with previous reports [40, 43, 44]. In the first cathodic scanning process, a broad hump centered around 0.8 V is attributed to the formation of solid electrolyte interface (SEI) layers and the reduction reaction of Sn nanocomplex with Li^+ to form Sn and Li_2O; the latter reaction is reversible and reflects a stable peak at 0.92 V in subsequent cycles [44–46]. The dominant peak below 0.5 V owes to electrochemical lithium storage by forming Li_xSn and trapping of Li^+ within the $Ti_3C_2T_x$ matrix, which are partially reversible and mainly responsible for sharp capacity decay at the first cycle [25, 40]. The reduction peaks are greatly different at subsequent scans compared with the first scan, suggesting the dynamic enhancement after the initial lithiation/delithiation activation combined with partially reversible reaction [28, 47]. In the anodic scanning, the dominant peak at approximately 0.54 V belongs to dealloying reaction of Li_xSn. Remarkably, two minor peaks are detected around 1.2 and 1.9 V, which are related to reversible conversion reaction of Sn to SnO and SnO to SnO_2, respectively [48, 49]. The good overlap of CV curves after the initial scan demonstrates the good reversibility and robustness of the STCT composite electrodes at subsequent cycles [28, 50].

The galvanostatic charging/discharging curves of STCT composites at different cycles are presented in Fig. 5b. The charging/discharging platforms have one-to-one corresponding relationship with the redox peaks in CV curves. The discharge and charge capacities of the first cycle are 1892.4 and 1291.7 mAh g^{-1}, respectively, with an initial coulombic efficiency of 68.3%. This value is relatively high among the $Ti_3C_2T_x$-based electrode materials [18, 21, 25, 40]. The irreversible capacity of the first cycle comes from unavoidable formation of SEI layer, irreversible conversion reaction of partial Sn nanocomplex, and irreversible capture of Li^+ in layered $Ti_3C_2T_x$ matrix [28, 40]. The coulombic efficiency rapidly climbs to 97.2% at the second cycle and remains stable above 99.7% during subsequent cycles. There is a descent in the initial 30 cycles, which may result from irreversible lithiation of $Ti_3C_2T_x$ MXene matrix (Fig. 5e, f) [50, 51]. The capacity stabilizes at about 745 mAh g^{-1} at 500 mA g^{-1} and no capacity decay in subsequent cycles, indicating the excellent electrochemical performance because of stable structure of STCT composites, which can work steadily over 1000 cycles with obvious electrochemical platforms (Figs. S14 and S19). SEM and TEM images of STCT electrodes after cycles are shown in Fig. S15, the cycled STCT electrodes remain stable structure, and no fissures can be observed at surface. Furthermore, the Sn nanocomplex particles are still dispersed uniformly at $Ti_3C_2T_x$ matrix after cycles, without agglomeration or pulverization (Fig. S16). The capacities of raw Ti_3AlC_2 material and multilayered $Ti_3C_2T_x$ are quite low under the same test conditions, only delivering about 60 and 121 mAh g^{-1} (Fig. S17). The multilayered STCT composites deliver a reversible capacity of 367.4 mAh g^{-1} after 100 cycles at 500 mA g^{-1} (Fig. S18), which is about triple of the capacity provided by individual multilayered $Ti_3C_2T_x$ without pillaring treatment. The result further demonstrates the significant effect of pillaring technique. An upward trend of capacity is observed upon cycling, especially in the

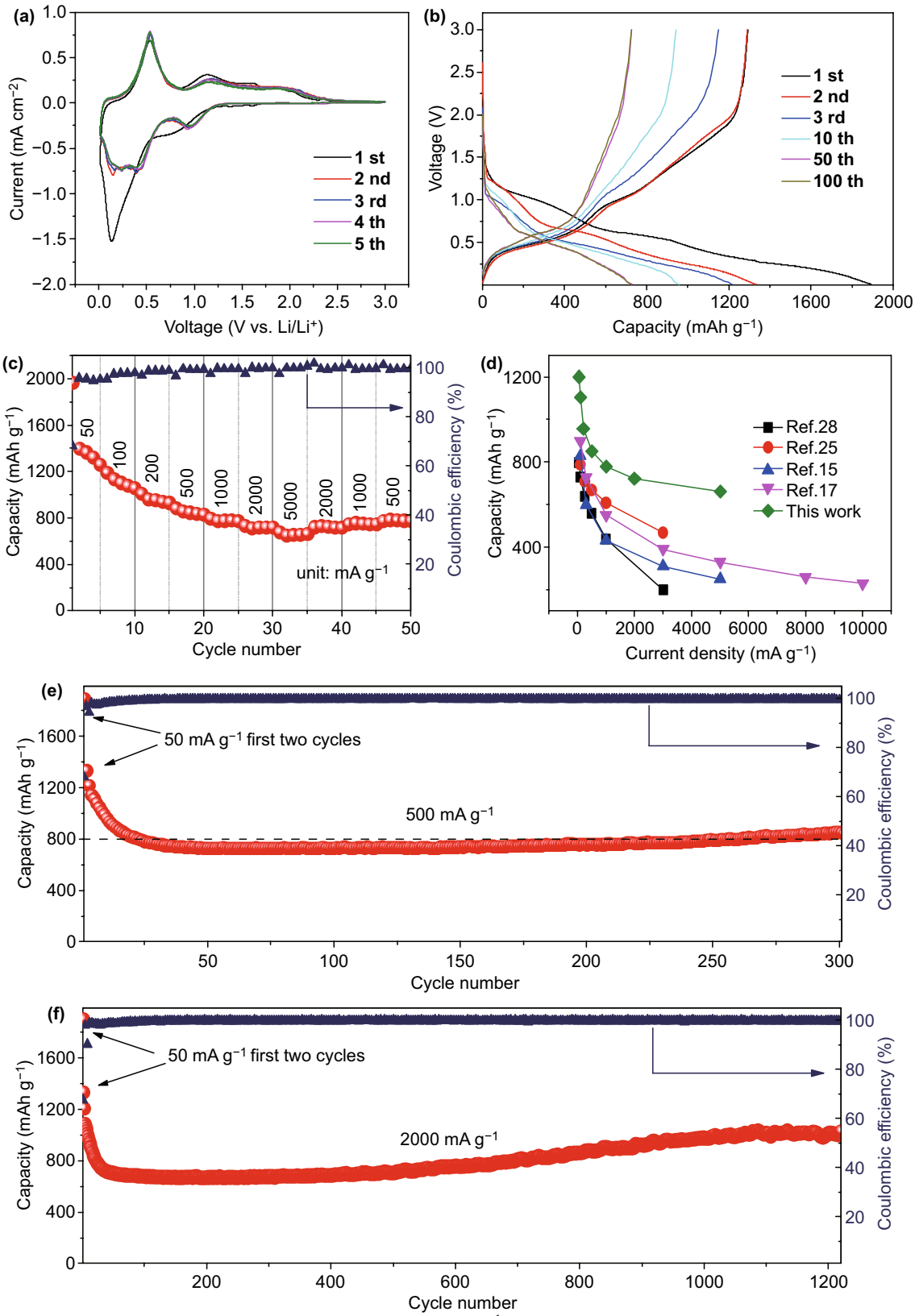

Fig. 5 Electrochemical results of STCT composites: **a** CV curves at 0.1 mV s^{-1}, **b** voltage–capacity curves of different cycles at 500 mA g^{-1}, and **c** rate performance. **d** Rate performance comparison of different pillared MXene-based anode materials reported recently (just focus on closely related pillared MXene-based composites), **e** cycle performance at 500 mA g^{-1}, and **f** long-term performance at a high current density of 2000 mA g^{-1}

https://doi.org/10.1007/s40820-020-0405-7

long-term cycling at 2000 mA g^{-1}. The capacity increases from 761.4 mAh g^{-1} at the 600th cycle to 1010.2 mAh g^{-1} at the 1075th cycle, giving a high capacity retention of 142% compared with the 40th cycle (Fig. S19). The uplift of capacity can be ascribed to the increased interlayer spacings of $Ti_3C_2T_x$ matrix [51–53], which are propped by the volume expansion of Sn nanocomplex during lithiation and persistent shuttle of ions and electrons in the interlayers, leading to continuous enhancement of lithium storage capacity of the composites upon cycling [25]. It is found that a higher current density can induce earlier uptrend of capacity due to more violent ion and electron flows, leading to faster expansion of the interlayer spacing (Fig. S20 and Table S1).

The rate performance of STCT electrode can be measured at different current densities from 50 to 5000 mA g^{-1} (Figs. 5c and S21). As the current density increases, the capacity decreases progressively. The stable discharging capacities at 500 and 5000 mAh g^{-1} are 881.5 and 662.2 mAh g^{-1}, respectively, indicating that the capacity remains up to 75.1% even the current density increases 10 times from 500 to 5000 mA g^{-1}. As the current density returns to 500 mA g^{-1}, the capacity recovers to 793.3 mAh g^{-1}, suggesting the good reversibility of the electrode (Fig. S21a–c). The electrode can still cycle steadily at 500 mA g^{-1} after rate test, indicating the stable structure during high-rate test (Fig. S21b). The outstanding rate performance mainly benefits from the ultrathin $Ti_3C_2T_x$ layers, the ultrafine Sn nanocomplex particles, and the "pillar effect" that caused increasing interlayer spacing of $Ti_3C_2T_x$ nanosheet matrix [28, 41, 54]. This rate capability and corresponding specific capacities in LIBs are much better than previous reports about pillared MXenes due to usage of few-layered MXenes without restacking phenomenon (Figs. 5d and S22) [15, 17, 25, 28], further demonstrating the effectiveness of NH^{4+} method and advantages of pillared few-layered MXenes.

In order to investigate reason for the excellent lithium storage of STCT composites, we analyzed the electrochemical kinetic mechanism by testing CV curves at various sweep speeds ranging from 0.1 to 2 mV s^{-1} (Fig. 6). As shown in Figs. 6a and S23a, b, a regular negative shift for the cathodic peaks and positive shift for the anodic peaks occur because of the polarization enhancement as the sweep speed increases [55]. The relationship between the peak current (i) and the scan rate (v) obeys the power law (Eqs. 1 and 2) [56]:

$$i = av^b \tag{1}$$

$$\log i = b\log v + \log a \tag{2}$$

where a and b are adjustable constants. The b value can reflect the dominant factor of the electrochemical process. When the b value is close to 1.0, the electrochemical reaction is mainly controlled by the surface capacitive effect, while when the b value is close to 0.5, a solid-state diffusion-controlled process should be dominant [57]. As shown in Fig. 6b, the b value can be determined through calculating the slope of the log(v)–log(i) plots. The b values for the cathodic and anodic processes are estimated to be 0.842 and 0.755 (Fig. S23c, d), respectively, indicating a more favored surface-dominated lithium storage mechanism of STCT electrode [58].

The capacity contributions from surface-dominated and diffusion-dominated processes can be further quantitatively analyzed through the analysis approach established by Dunn et al. [59]. The current response of CV scan at a potential (V) varies with the scan rate (v) and obeys Eq. 3:

$$i(V) = k_1 v + k_2 v^{1/2} \tag{3}$$

$k_1 v$ and $k_2 v^{1/2}$, respectively, represent the capacitive and diffusion-dominated processes [60] where k_1 and k_2 are adjustable constants. Figure 6c shows the typical quantitative separation of capacitive current response compared with the total current response at a scan rate of 0.1 mV s^{-1}. The capacitive effect contribution (black-shaded area) composes about 52.94% of the total capacity (red line surrounded area). As the scan rate rises from 0.1 to 2 mV s^{-1}, the capacitive contribution proportion gradually increases from 52.94 to 86.96%. The analysis result manifests the important role of capacitive lithium storage process, especially at high current densities. The high proportion of surface-controlled process implies the short ion transport path and efficient charge transfer kinetics, thereby pledging the excellent rate capability and superior cycling stability. The electrochemical kinetic result well explains the excellent electrochemical performance of STCT composites and further testifies the superior kinetic characteristics of pillared few-layered $Ti_3C_2T_x$ MXenes.

Based on the characterization and electrochemical test results, benefited from "pillar effect," the pillared few-layered $Ti_3C_2T_x$ nanosheets are ideal carrier for Sn nanocomplex; STCT composites were synthesized successfully and show outstanding electrochemical performance, which can be attributed to the following reasons: (1) The pillared few-layered $Ti_3C_2T_x$ matrix with enlarged interlayer

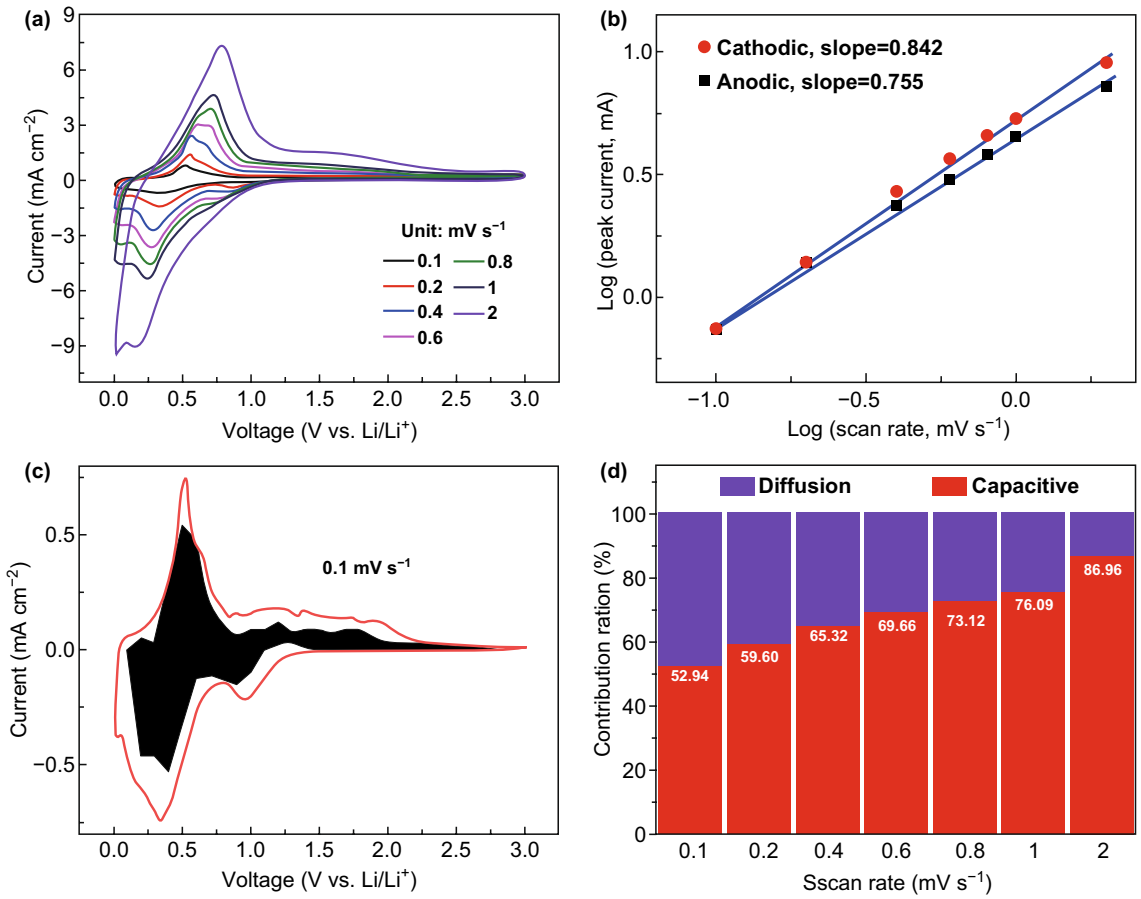

Fig. 6 **a** CV curves of STCT electrodes at different scan rates from 0.1 to 2 mV s^{-1}. **b** Plots for log (*i*) versus log (*v*), where *i* is the peak current and *v* is the scan rate. **c** Capacitive contribution proportion compared with the total current response at 0.1 mA s^{-1}. **d** Bar charts of the capacitive contribution proportion at different scan rates (from 0.1 to 2 mV s^{-1})

spacing behaves as efficient lithium storage container [28], which can also act as 2D conductive network to enhance the electron transfer and Li^+ transport [61, 62]. (2) The $Ti_3C_2T_x$ can effectively confine the Sn nanocomplex particles within interlayer and work as a flexible skeleton to keep the structural stability of the composites during cycling process. (3) In addition, the ultrasmall Sn nanocomplex dots further reinforce the kinetics properties [63]. Therefore, the conversion reaction of Sn oxide is partially reversible in STCT composites. The reversible utilization of Li_2O can not only increase the specific capacity of the electrode, but also improve the coulombic efficiency [64, 65]. (4) The atomic Sn nanocomplex particles are anchored into the few-layered $Ti_3C_2T_x$ matrix through electrostatic or chemical adsorption via formation of Sn–O–Ti bonding; the grain growth and aggregation of the particles are thoroughly restrained. The Sn nanocomplex can act as ideal pillaring agent to significantly improve the capacity of $Ti_3C_2T_x$, because the drastic volume fluctuation during lithiation/delithiation will further pry the interlayer of $Ti_3C_2T_x$ and acquire more lithium storage interspace, leading to fascinating electrochemical performance, especially rate performance. As far as we know, the STCT composites exhibit the best electrochemical performance among tin-based materials/MXene composites reported so far, and one of the best among the MXene-based materials (Table S2). Pillared few-layered MXenes can provide enlightenment for the insightful development of pillared MXenes, which open a new path for the application of MXenes due to larger interlayer spacing. In the future, it is believed the MXenes of $n = 3$ in chemical formula ($M_{n+1}C_nT_x$) are more attractive because of intrinsic larger interlayer spacing (1.4 nm) than that of $n = 2$ (1 nm) or $n = 1$ (0.7 nm) [15, 25, 66–69].

https://doi.org/10.1007/s40820-020-0405-7

4 Conclusions

In summary, we design a facile NH^{4+} method to fundamentally solve the restacking phenomenon of few-layered MXenes, which is important for further study of various MXenes. Besides, partial atomic Sn nanocomplex pillared few-layered $Ti_3C_2T_x$ composite (STCT) was fabricated by CTAB pre-pillaring and Sn nanocomplex pillaring process. The pillared few-layered structure is deemed responsible for the superior electrochemical performance of the as-prepared MXene-based material. The novel few-layered structure will not only facilitate the full utilization of $Ti_3C_2T_x$ in lithium storage, but also improves the dynamic properties of decorated Sn nanocomplex. The ingenious combination of $Ti_3C_2T_x$ and Sn nanocomplex can generate "pillar effect." On the one hand, the highly conductive $Ti_3C_2T_x$ can effectually restrain Sn nanocomplex particle growth and agglomeration, thereby ensuring the high use ratio of Sn nanocomplex and activating reversible conversion reaction of Sn back to Sn oxide. On the other hand, the large volume expansion of Sn nanocomplex during charging/discharging processes will further open the interlayers of $Ti_3C_2T_x$ and allow more Li^+ storage; as a result, Sn nanocomplex pillared few-layered $Ti_3C_2T_x$ composite exhibits outstanding electrochemical performance: It delivers a stable discharging capacity about 800 mAh g^{-1} at 500 mA g^{-1} and maintains 1016 mAh g^{-1} after 1200 cycles at 2000 mA g^{-1}. A high capacity retention of 680 mAh g^{-1} is also obtained at 5 A g^{-1}, suggesting remarkable rate ability of STCT composites. Our work demonstrates the pillared few-layered MXene nanosheets are ideal matrix for high capacity anode materials with large volume expansion. We believe this work can provide enlightenment for the modification of other energy storage materials.

Acknowledgements The authors are grateful for the financial support by the National Natural Science Foundation of China (Grant No. 51901206, 51822104) and the Training Program of Major Basic Research Project of Provincial Natural Science Foundation of Guangdong (2017B030308001).

Electronic supplementary material The online version of this article (https://doi.org/10.1007/s40820-020-0405-7) contains supplementary material, which is available to authorized users.

References

1. H.J. Yoon, J.H. Yang, Z. Zhou, S.S. Yang, M.M.-C. Cheng, Carbon dioxide gas sensor using a graphene sheet. Sens. Actuat. B **157**(1), 310–313 (2011). https://doi.org/10.1016/j.snb.2011.03.035
2. P. Li, J.Y. Jeong, B. Jin, K. Zhang, J.H. Park, Vertically oriented MoS_2 with spatially controlled geometry on nitrogenous graphene sheets for high-performance sodium-ion batteries. Adv. Energy Mater. **8**(19), 1703300 (2018). https://doi.org/10.1002/aenm.201703300
3. A. Kuang, T. Zhou, G. Wang, Y. Li, G. Wu, H. Yuan, H. Chen, X. Yang, Dehydrogenation of ammonia borane catalyzed by pristine and defective h-BN sheets. Appl. Surf. Sci. **362**, 562–571 (2016). https://doi.org/10.1016/j.apsusc.2015.11.011
4. C. Tan, X. Cao, X.-J. Wu, Q. He, J. Yang et al., Recent advances in ultrathin Two-dimensional nanomaterials. Chem. Rev. **117**(9), 6225–6331 (2017). https://doi.org/10.1021/acs.chemrev.6b00558
5. M. Naguib, M. Kurtoglu, V. Presser, J. Lu, J. Niu et al., Two-dimensional nanocrystals produced by exfoliation of Ti_3AlC_2. Adv. Mater. **23**(37), 4248–4253 (2011). https://doi.org/10.1002/adma.201102306
6. M. Naguib, O. Mashtalir, J. Carle, V. Presser, J. Lu, L. Hultman, Y. Gogotsi, M.W. Barsoum, Two-dimensional transition metal carbides. ACS Nano **6**(2), 1322–1331 (2012). https://doi.org/10.1021/nn204153h
7. W. Sun, S.A. Shah, Y. Chen, Z. Tan, H. Gao, T. Habib, M. Radovic, M.J. Green, Electrochemical etching of Ti_2AlC to Ti_2CT_x (MXene) in low-concentration hydrochloric acid solution. J. Mater. Chem. A **5**(41), 21663–21668 (2017). https://doi.org/10.1039/C7TA05574A
8. D. Sun, M. Wang, Z. Li, G. Fan, L.-Z. Fan, A. Zhou, Two-dimensional Ti_3C_2 as anode material for Li–ion batteries. Electrochem. Commun. **47**, 80–83 (2014). https://doi.org/10.1016/j.elecom.2014.07.026
9. N.K. Chaudhari, H. Jin, B. Kim, D. San Baek, S.H. Joo, K. Lee Mxene, An emerging Two-dimensional material for future energy conversion and storage applications. J. Mater. Chem. A **5**(47), 24564–24579 (2017). https://doi.org/10.1039/C7TA09094C

10. C. Zhan, M. Naguib, M. Lukatskaya, P.R.C. Kent, Y. Gogotsi, D.-E. Jiang, Understanding the MXene pseudocapacitance. J. Phys. Chem. Lett. **9**(6), 1223–1228 (2018). https://doi.org/10.1021/acs.jpclett.8b00200
11. L. Huan, Z. Xin, Z. Yifan, C. Bin, Z. Qizhen et al., Electrostatic self-assembly of 0d–2d SnO_2 quantum dots/$Ti_3C_2T_x$ MXene hybrids as anode for lithium-ion batteries. Nano-Micro Lett. **11**, 65 (2019). https://doi.org/10.1007/s40820-019-0296-7
12. Z. Peng, W. Danjun, Z. Qizhen, S. Ning, F. Feng, X. Bin, Plate-to-layer Bi_2MoO_6/MXene heterostructure as high performance anode material for lithium ion batteries. Nano-Micro Lett. **11**, 81 (2019). https://doi.org/10.1007/s40820-019-0312-y
13. Z. Fu, N. Wang, D. Legut, C. Si, Q. Zhang et al., Rational design of flexible Two-dimensional mxenes with multiple functionalities. Chem. Rev. **119**(23), 11980–12031 (2019). https://doi.org/10.1021/acs.chemrev.9b00348
14. Q. Tang, Z. Zhou, P. Shen, Are MXenes promising anode materials for Li ion batteries? Computational studies on electronic properties and Li storage capability of Ti_3C_2 and $Ti_3C_2X_2$ (X=F, OH) monolayer. J. Am. Chem. Soc. **134**(40), 16909–16916 (2012). https://doi.org/10.1021/ja308463r
15. C. Wang, H. Xie, S. Chen, B. Ge, D. Liu et al., Atomic cobalt covalently engineered interlayers for superior lithium-ion storage. Adv. Mater. **30**(32), 1802525 (2018). https://doi.org/10.1002/adma.201802525
16. M. Malaki, A. Maleki, R.S. Varma, MXenes and ultrasonication. J. Mater. Chem. A **7**(18), 10843–10857 (2019). https://doi.org/10.1039/C9TA01850F
17. C. Wang, S. Chen, H. Xie, S. Wei, C. Wu, L. Song, Atomic Sn^{4+} decorated into vanadium carbide MXene interlayers for superior lithium storage. Adv. Energy Mater. **9**(4), 1802977 (2019). https://doi.org/10.1002/aenm.201802977
18. J. Luo, J. Zheng, J. Nai, C. Jin, H. Yuan et al., Atomic sulfur covalently engineered interlayers of Ti_3C_2 MXene for ultrafast sodium-ion storage by enhanced pseudocapacitance. Adv. Funct. Mater. **29**(10), 1808107 (2019). https://doi.org/10.1002/adfm.201808107
19. S. Zheng, C. Zhang, F. Zhou, Y. Dong, X. Shi, V. Nicolosi, Z.-S. Wu, X. Bao, Ionic liquid pre-intercalated mxene films for ionogel-based flexible micro-supercapacitors with high volumetric energy density. J. Mater. Chem. A **7**(16), 9478–9485 (2019). https://doi.org/10.1039/C9TA02190F
20. M.Q. Zhao, X. Xie, C.E. Ren, T. Makaryan, B. Anasori, G. Wang, Y. Gogotsi, Hollow MXene spheres and 3D macroporous MXene frameworks for Na-ion storage. Adv. Mater. **29**(37), 1702410 (2017). https://doi.org/10.1002/adma.201702410
21. Z. Ma, X. Zhou, W. Deng, D. Lei, Z. Liu, 3D porous MXene (Ti_3C_2)/reduced graphene oxide hybrid films for advanced lithium storage. ACS Appl. Mater. Interfaces **10**(4), 3634–3643 (2018). https://doi.org/10.1021/acsami.7b17386
22. Y. Wang, H. Dou, J. Wang, B. Ding, Y. Xu, Z. Chang, X. Hao, Three-dimensional porous MXene/layered double hydroxide composite for high performance supercapacitors. J. Power Sources **327**, 221–228 (2016). https://doi.org/10.1016/j.jpowsour.2016.07.062
23. X. Xie, M.-Q. Zhao, B. Anasori, K. Maleski, C.E. Ren et al., Porous heterostructured MXene/carbon nanotube composite paper with high volumetric capacity for sodium-based energy storage devices. Nano Energy **26**, 513–523 (2016). https://doi.org/10.1016/j.nanoen.2016.06.005
24. M.R. Lukatskaya, O. Mashtalir, C.E. Ren, Y. Dall'Agnese, P. Rozier et al., Cation intercalation and high volumetric capacitance of two-dimensional titanium carbide. Science **341**(6153), 1502–1505 (2013). https://doi.org/10.1126/science.1241488
25. J. Luo, W. Zhang, H. Yuan, C. Jin, L. Zhang et al., Pillared structure design of MXene with ultralarge interlayer spacing for high-performance lithium-ion capacitors. ACS Nano **11**(3), 2459–2469 (2017). https://doi.org/10.1021/acsnano.6b07668
26. Z. Ling, C.E. Ren, M.-Q. Zhao, J. Yang, J.M. Giammarco, J. Qiu, M.W. Barsoum, Y. Gogotsi, Flexible and conductive MXene films and nanocomposites with high capacitance. Proc. Natl. Acad. Sci. U.S.A. **111**(47), 16676–16681 (2014). https://doi.org/10.1073/pnas.1414215111
27. M.-Q. Zhao, M. Torelli, C.E. Ren, M. Ghidiu, Z. Ling, B. Anasori, M.W. Barsoum, Y. Gogotsi, 2D titanium carbide and transition metal oxides hybrid electrodes for Li–ion storage. Nano Energy **30**, 603–613 (2016). https://doi.org/10.1016/j.nanoen.2016.10.062
28. J. Luo, X. Tao, J. Zhang, Y. Xia, H. Huang et al., Sn^{4+} ion decorated highly conductive Ti_3C_2 MXene: promising lithium-ion anodes with enhanced volumetric capacity and cyclic performance. ACS Nano **10**(2), 2491–2499 (2016). https://doi.org/10.1021/acsnano.5b07333
29. J. Luo, C. Wang, H. Wang, X. Hu, E. Matios et al., Pillared MXene with ultralarge interlayer spacing as a stable matrix for high performance sodium metal anodes. Adv. Funct. Mater. **29**(3), 1805946 (2019). https://doi.org/10.1002/adfm.201805946
30. M. Xu, S. Lei, J. Qi, Q. Dou, L. Liu et al., Opening magnesium storage capability of two-dimensional MXene by intercalation of cationic surfactant. ACS Nano **12**(4), 3733–3740 (2018). https://doi.org/10.1021/acsnano.8b00959
31. V.M. Hong Ng, H. Huang, K. Zhou, P.S. Lee, W. Que, J.Z. Xu, L.B. Kong, Recent progress in layered transition metal carbides and/or nitrides (MXenes) and their composites: synthesis and applications. J. Mater. Chem. A **5**(7), 3039–3068 (2017). https://doi.org/10.1039/C6TA06772G
32. H. Zhang, Ultrathin two-dimensional nanomaterials. ACS Nano **9**(10), 9451–9469 (2015). https://doi.org/10.1021/acsnano.5b05040
33. Y. Wu, P. Nie, J. Wang, H. Dou, X. Zhang, Few-layer MXenes delaminated via high-energy mechanical milling for enhanced sodium-ion batteries performance. ACS Appl. Mater. Interfaces **9**(45), 39610–39617 (2017). https://doi.org/10.1021/acsami.7b12155
34. H. Huang, J. Cui, G. Liu, R. Bi, L. Zhang, Carbon-coated $MoSe_2$/MXene hybrid nanosheets for superior potassium

 https://doi.org/10.1007/s40820-020-0405-7

storage. ACS Nano **13**(3), 3448–3456 (2019). https://doi.org/10.1021/acsnano.8b09548

35. C. Zeng, F. Xie, X. Yang, M. Jaroniec, L. Zhang, S.-Z. Qiao, Ultrathin titanate nanosheets/graphene films derived from confined transformation for excellent Na/K ion storage. Angew. Chem. Int. Ed. **57**(28), 8540–8544 (2018). https://doi.org/10.1002/anie.201803511
36. C. Eames, M.S. Islam, Ion intercalation into Two-dimensional transition-metal carbides: global screening for new high-capacity battery materials. J. Am. Chem. Soc. **136**(46), 16270–16276 (2014). https://doi.org/10.1021/ja508154e
37. R. Fang, C. Lu, A. Chen, K. Wang, H. Huang et al., 2D MXene-based energy storage materials: interfacial structure design and functionalization. Chemsuschem **12**, 1–12 (2019). https://doi.org/10.1002/cssc.201902537
38. V. Natu, M. Clites, E. Pomerantseva, M.W. Barsoum, Mesoporous MXene powders synthesized by acid induced crumpling and their use as Na-ion battery anodes. Mater. Res. Lett. **6**(4), 230–235 (2018). https://doi.org/10.1080/21663831.2018.1434249
39. H. Zhang, L. Cong, J. Wang, X. Wang, G. Liu et al., Impact of CTAB on morphology and electrochemical performance of MoS_2 nanoflowers with improved lithium storage properties. J. Mater. Sci.: Mater. Electron. **29**(5), 3631–3639 (2018). https://doi.org/10.1007/s10854-017-8293-4
40. D. Zuo, S. Song, C. An, L. Tang, Z. He, J. Zheng, Synthesis of sandwich-like structured Sn/SnO_x@MXene composite through in situ growth for highly reversible lithium storage. Nano Energy **62**, 401–409 (2019). https://doi.org/10.1016/j.nanoen.2019.05.062
41. H. Ying, S. Zhang, Z. Meng, Z. Sun, W.-Q. Han, Ultrasmall Sn nanodots embedded inside N-doped carbon microcages as high-performance lithium and sodium ion battery anodes. J. Mater. Chem. A **5**(18), 8334–8342 (2017). https://doi.org/10.1039/C7TA01480E
42. Y.T. Liu, P. Zhang, N. Sun, B. Anasori, Q.Z. Zhu, H. Liu, Y. Gogotsi, B. Xu, Self-assembly of transition metal oxide nanostructures on MXene nanosheets for fast and stable lithium storage. Adv. Mater. **30**(23), 1707334 (2018). https://doi.org/10.1002/adma.201707334
43. B. Ahmed, D.H. Anjum, Y. Gogotsi, H.N. Alshareef, Atomic layer deposition of SnO_2 on MXene for Li–ion battery anodes. Nano Energy **34**, 249–256 (2017). https://doi.org/10.1016/j.nanoen.2017.02.043
44. J. Sun, L. Xiao, S. Jiang, G. Li, Y. Huang, J. Geng, Fluorine-doped SnO_2@graphene porous composite for high capacity lithium-ion batteries. Chem. Mater. **27**(13), 4594–4603 (2015). https://doi.org/10.1021/acs.chemmater.5b00885
45. X.S. Zhou, L.J. Wan, Y.G. Guo, Binding SnO_2 nanocrystals in nitrogen-doped graphene sheets as anode materials for lithium-ion batteries. Adv. Mater. **25**(15), 2152–2157 (2013). https://doi.org/10.1002/adma.201300071
46. Z. Li, G. Wu, S. Deng, S. Wang, Y. Wang et al., Combination of uniform SnO_2 nanocrystals with nitrogen doped graphene for high-performance lithium-ion batteries anode. Chem. Eng. J. **283**, 1435–1442 (2016). https://doi.org/10.1016/j.cej.2015.08.052
47. C. Wang, G. Du, K. Ståhl, H. Huang, Y. Zhong, J. Jiang, Ultrathin SnO_2 nanosheets: oriented attachment mechanism, nonstoichiometric defects, and enhanced lithium-ion battery performances. J. Phys. Chem. C **116**(6), 4000–4011 (2012). https://doi.org/10.1021/jp300136p
48. G. Wen, H. Liu, T. Liang, Y. Ouyang, L. Tan et al., Good cycling stability and high initial efficiency demonstrated in full cells with limited lithium source for an advanced SnO_2–Co–C composite anode. Electrochim. Acta **334**, 135640 (2020). https://doi.org/10.1016/j.electacta.2020.135640
49. T. Liang, R. Hu, H. Zhang, H. Zhang, H. Wang et al., A scalable ternary SnO_2–Co–C composite as a high initial coulombic efficiency, large capacity and long lifetime anode for lithium ion batteries. J. Mater. Chem. A **6**(16), 7206–7220 (2018). https://doi.org/10.1039/C8TA00957K
50. H. Ying, F. Xin, W. Han, Structural evolution of 3D nano-Sn/reduced graphene oxide composite from a sandwich-like structure to a curly Sn@carbon nanocage-like structure during lithiation/delithiation cycling. Adv. Mater. Interfaces **3**(19), 1600498 (2016). https://doi.org/10.1002/admi.201600498
51. R. Meng, J. Huang, Y. Feng, L. Zu, C. Peng et al., Black phosphorus quantum dot/Ti_3C_2 MXene nanosheet composites for efficient electrochemical lithium/sodium-ion storage. Adv. Energy Mater. **8**(26), 1801514 (2018). https://doi.org/10.1002/aenm.201801514
52. C. Zhang, X. Wang, Q. Liang, X. Liu, Q. Weng et al., Amorphous phosphorus/nitrogen-doped graphene paper for ultrastable sodium-ion batteries. Nano Lett. **16**(3), 2054–2060 (2016). https://doi.org/10.1021/acs.nanolett.6b00057
53. J. Luo, X. Xia, Y. Luo, C. Guan, J. Liu et al., Rationally designed hierarchical TiO_2@Fe_2O_3 hollow nanostructures for improved lithium ion storage. Adv. Energy Mater. **3**(6), 737–743 (2013). https://doi.org/10.1002/aenm.201200953
54. J. Xiong, L. Pan, H. Wang, F. Du, Y. Chen, J. Yang, C.J. Zhang, Synergistically enhanced lithium storage performance based on titanium carbide nanosheets (MXene) backbone and SnO_2 quantum dots. Electrochim. Acta **268**, 503–511 (2018). https://doi.org/10.1016/j.electacta.2018.02.090
55. W. Yao, S. Wu, L. Zhan, Y. Wang, Two-dimensional porous carbon-coated sandwich-like mesoporous SnO_2/graphene/mesoporous SnO_2 nanosheets towards high-rate and long cycle life lithium-ion batteries. Chem. Eng. J. **361**, 329–341 (2019). https://doi.org/10.1016/j.cej.2018.08.217
56. B.K. Lesel, J.S. Ko, B. Dunn, S.H. Tolbert, Mesoporous $LixMn_2O_4$ thin film cathodes for lithium-ion pseudocapacitors. ACS Nano **10**(8), 7572–7581 (2016). https://doi.org/10.1021/acsnano.6b02608
57. G.A. Muller, J.B. Cook, H.-S. Kim, S.H. Tolbert, B. Dunn, High performance pseudocapacitor based on 2D layered metal chalcogenide nanocrystals. Nano Lett. **15**(3), 1911–1917 (2015). https://doi.org/10.1021/nl504764m
58. Y. Dong, M. Hu, Z. Zhang, J.A. Zapien, X. Wang, J.-M. Lee, W. Zhang, Nitrogen-doped carbon-encapsulated antimony

sulfide nanowires enable high rate capability and cyclic stability for sodium-ion batteries. ACS Appl. Nano Mater. **2**(3), 1457–1465 (2019). https://doi.org/10.1021/acsanm.8b02335

59. V. Augustyn, J. Come, M.A. Lowe, J.W. Kim, P.-L. Taberna et al., High-rate electrochemical energy storage through Li^+ intercalation pseudocapacitance. Nat. Mater. **12**(6), 518 (2013). https://doi.org/10.1038/nmat3601
60. D. Chao, C. Zhu, P. Yang, X. Xia, J. Liu et al., Array of nanosheets render ultrafast and high-capacity Na-ion storage by tunable pseudocapacitance. Nat. Commun. **7**, 12122 (2016). https://doi.org/10.1038/ncomms12122
61. X. Liang, A. Garsuch, L.F. Nazar, Sulfur cathodes based on conductive MXene nanosheets for high-performance lithium–sulfur batteries. Angew. Chem. Int. Ed. **54**(13), 3907–3911 (2015). https://doi.org/10.1002/anie.201410174
62. Y. Wang, Y. Li, Z. Qiu, X. Wu, P. Zhou et al., Fe_3O_4@ Ti_3C_2 MXene hybrids with ultrahigh volumetric capacity as an anode material for lithium-ion batteries. J. Mater. Chem. A **6**(24), 11189–11197 (2018). https://doi.org/10.1039/C8TA00122G
63. B. Zhang, J. Huang, J.K. Kim, Ultrafine amorphous SnO_x embedded in carbon nanofiber/carbon nanotube composites for Li–ion and Na–ion batteries. Adv. Funct. Mater. **25**(32), 5222–5228 (2015). https://doi.org/10.1002/adfm.201501498
64. R. Hu, D. Chen, G. Waller, Y. Ouyang, Y. Chen et al., Dramatically enhanced reversibility of Li_2O in SnO_2-based electrodes: the effect of nanostructure on high initial reversible capacity. Energy Environ. Sci. **9**(2), 595–603 (2016). https://doi.org/10.1039/C5EE03367E
65. R. Hu, H. Zhang, Z. Lu, J. Liu, M. Zeng, L. Yang, B. Yuan, M. Zhu, Unveiling critical size of coarsened sn nanograins for achieving high round-trip efficiency of reversible conversion reaction in lithiated SnO_2 nanocrystals. Nano Energy **45**, 255–265 (2018). https://doi.org/10.1016/j.nanoen.2018.01.007
66. H. Li, X. Wang, H. Li, S. Lin, B. Zhao et al., Capacitance improvements of $V_4C_3T_x$ by NH_3 annealing. J. Alloys Compd. **784**, 923–930 (2019). https://doi.org/10.1016/j.jallcom.2019.01.111
67. J. Zhou, S. Lin, Y. Huang, P. Tong, B. Zhao, X. Zhu, Y. Sun, Synthesis and lithium ion storage performance of two-dimensional V_4C_3 MXene. Chem. Eng. J. **373**, 203–212 (2019). https://doi.org/10.1016/j.cej.2019.05.037
68. X. Wang, H. Li, H. Li, S. Lin, J. Bai et al., Heterostructures of Ni–Co–Al layered double hydroxide assembled on V_4C_3 MXene for high-energy hybrid supercapacitors. J. Mater. Chem. A **7**(5), 2291–2300 (2019). https://doi.org/10.1039/C8TA11249E
69. J. Bai, B. Zhao, S. Lin, K. Li, J. Zhou, J. Dai, X. Zhu, Y. Sun, Construction of hierarchical V_4C_3-MXene/MoS_2/C nanohybrids for high rate lithium-ion batteries. Nanoscale **12**(2), 1144–1154 (2020). https://doi.org/10.1039/C9NR07646H

 https://doi.org/10.1007/s40820-020-0405-7